SUPPLEMENTAL DOCUMENT: Sub-nanosecond all-optically reconfigurable photonics in optical fibres

KUNHAO JI[1,*], DAVID J. RICHARDSON[1,2], STEFAN WABNITZ[3], AND MASSIMILIANO GUASONI[1,*]

[1]Optoelectronics Research Centre, University of Southampton, Southampton SO17 1BJ, United Kingdom
[2]Microsoft (Lumenisity Limited), Unit 7, The Quadrangle, Abbey Park Industrial Estate, Romsey, SO51 9DL, United Kingdom
[3]Department of Information Engineering, Electronics and Telecommunications (DIET), Sapienza University of Rome, 00184 Rome, Italy
*m.guasoni@soton.ac.uk

Supplementary Information 1: Fibre modes and coefficients

In Fig. S1, we present the spatial profiles of the modes of the fibres tested in our experiments: a homemade dual-core fibre (DCF) and three-core fibre (TCF) supporting respectively 2 and 3 guided modes; and then a polarization-maintaining (PM) few-mode fibre (PM1550-xp from Thorlabs) and a highly nonlinear PM few-mode fibre (PMHN1 from Thorlabs) supporting 3 guided modes. Note that, in our experiments, the DCF is used both as bimodal fibre to illustrate multimode manipulation (Figs. 3 and 6 of the manuscript) and as multicore fibre for multicore manipulation (Fig. 4 of the manuscript). Modes M_1 and M_2 in the DCF correspond to the supermodes with the core fields in phase and anti-phase, respectively. Modes M_1, M_2 and M_3 in the PM1550-xp and PMHN1 fibre correspond to the standard linearly polarized modes LP_{01}, LP_{11e}, and LP_{11o}, respectively. Note that in these fibres LP_{11e} and LP_{11o} are non-degenerate.

Tables S1 and S2 list the Kerr coefficients and inverse group velocities for the fibres under test. These coefficients, along with the spatial profiles of the modes, were computed using finite element method simulations (central wavelength λ_c =1040 nm).

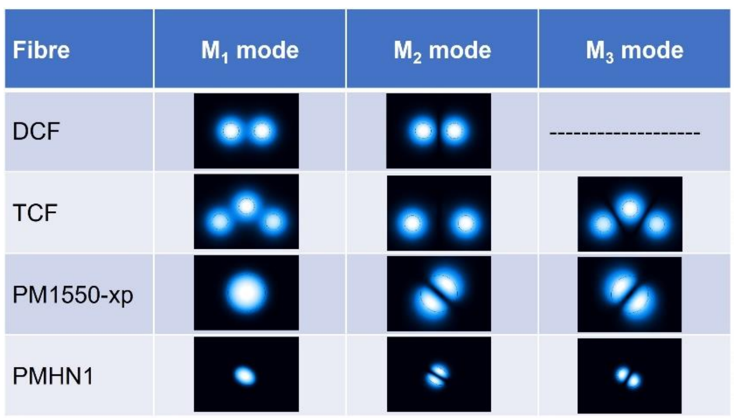

Fig. S1. Modes of the fibres under test. Spatial distribution (intensity) computed from finite element method simulations.

Table S1: Kerr coefficients

Fibre	γ_{11}(W^{-1}km^{-1})	γ_{22}(W^{-1}km^{-1})	γ_{33}(W^{-1}km^{-1})	$\gamma_{12}=\gamma_{21}$(W^{-1}km^{-1})	$\gamma_{13}=\gamma_{31}$(W^{-1}km^{-1})	$\gamma_{23}=\gamma_{32}$(W^{-1}km^{-1})
DCF	3.00	3.12	---	3.06	---	---
TCF	2.30	3.17	2.46	1.56	2.37	1.61
PM1550-xp	3.00	2.59	2.44	1.73	1.67	0.84
PMHN1	13.20	12.50	10.71	8.41	7.32	3.84

Table S2: Inverse group velocity v_n^{-1} of mode-n

Fibre	v_1^{-1} (ns/m)	$v_2^{-1} - v_1^{-1}$ (ps/m)	$v_3^{-1} - v_1^{-1}$ (ps/m)
DCF	4.906	1.068	------

TCF	4.906	0.714	1.513
PM1550-xp	4.895	0.452	0.516
PMHN1	4.978	11.919	0.744

Supplementary Information 2: Tuneable mode manipulation in three-mode fibres

Mode manipulation has been tested experimentally in two three-mode commercial fibres from Thorlabs, namely PM1550-xp and PMHN1. Both these fibres support the propagation of LP_{01}, LP_{11e} and LP_{11o} modes at a wavelength λ_c=1040 nm. The length of the test fibres is ~0.4m, and the probe and BCB are co-polarized.

Fig. S2a-c display the output probe mode distribution as a function of the BCB peak power in the PM1550-xp fibre and in three distinct cases. By adjusting the BCB mode distribution (reported at the top of each panel) we trigger different dynamics in the output probe. In Fig.S2a, the power exchange between the LP_{01} and LP_{11o} modes is promoted. For a BCB peak power of ~11kW, the output probe exhibits approximately equal power distribution between the LP_{01} and LP_{11o} modes. On the contrary, in Fig.S2b, the power exchange between the LP_{01} and LP_{11e} modes is favoured. Finally, in Fig.S2c we observe power exchange between all the 3 modes. Now, for a BCB peak power of ~11 kW, the output probe exhibits approximately equal power distribution between all the 3 modes.

Fig. S2d,e display the results in the PMHN1 fibre in two distinct instances. The input probe mode state is similar in both cases, and BCB mode distribution is properly adjusted to trigger different dynamics, with most of the output probe power redirected either on mode LP_{01} (Fig. S2d) or LP_{11o} (Fig. S2e). It is worth noting that the BCB peak power required to achieve relevant dynamics is substantially lower than in the case of the PM1550-xp, being as small as ~1kW. This is essentially due to the high nonlinearity of the fibre. The Kerr coefficients are indeed substantially larger in the PMHN1 fibre than in the PM1550-xp fibre (see Table S1).

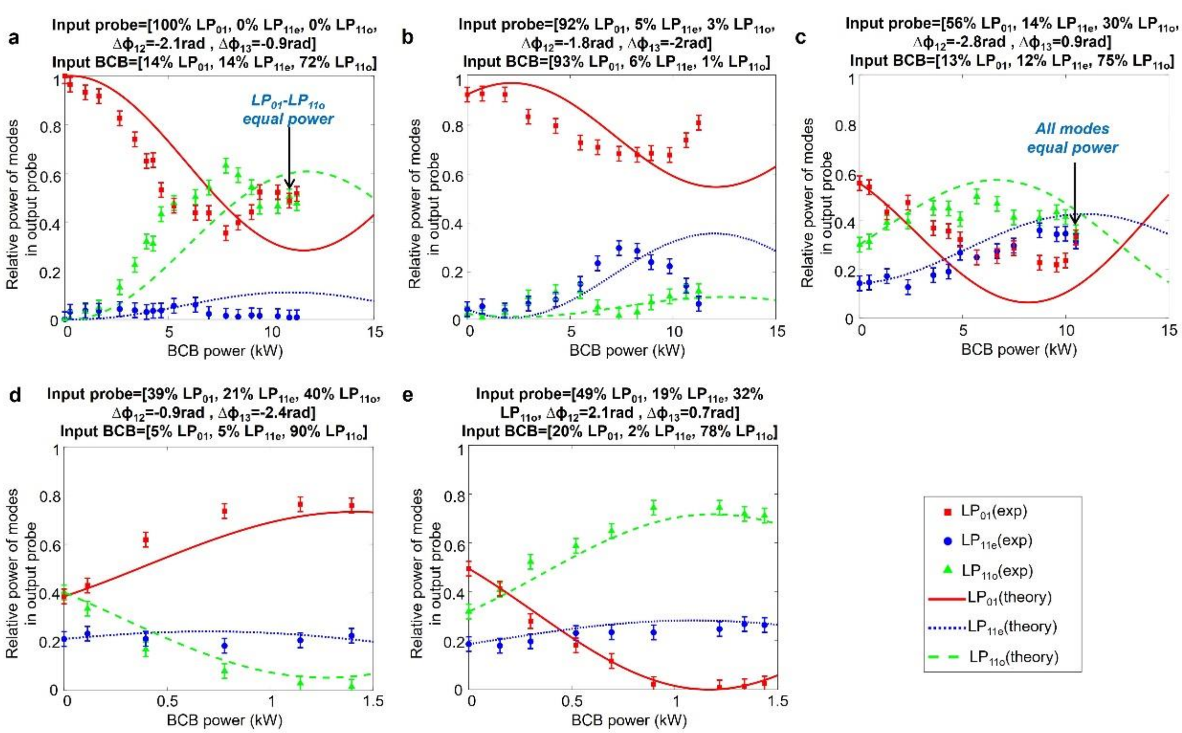

Fig. S2. Tuneable mode manipulation in three-mode fibres (PM1550-xp and PMHN1). a-**c**. Mode decomposition of the output probe as a function of the BCB peak power for the PM1550-xp fibre. Input probe mode state and BCB mode distribution are reported at the top of each panel. **d**,**e**. Same as panel a-c but for the HNF1 fibre. Exp=experimental results; Theory= theoretical results from solution of equation (1) in the main manuscript. Error bars of ±3% are added to the measured relative power of each mode, which represents the estimated uncertainty of our mode decomposition algorithm.

Supplementary Information 3: Mode manipulation via probe-BCB relative polarization

The relative polarization between input probe and BCB represents a further parameter to all-optically reconfigure the output probe. Fig. S3 illustrates some experimental results in the case of a bimodal fibre (DCF). The evolution of the output probe mode distribution as a function of the BCB power is reported when input probe and BCB are either co-polarized (Fig. S3a) or orthogonally polarized (Fig. S3b) and while maintaining the same input probe and BCB mode state. In the case of orthogonal polarization, we observe a slower modal conversion dynamic, due to the weaker interaction between the probe and the BCB (coefficient κ is reduced by a factor of 1/3 in equation (4) of the manuscript). Fig. S3c shows the mode distribution of the output probe when the probe-BCB relative polarization is continually adjusted from 0 deg (co-polarized) to 90 deg (orthogonally polarized), whereas the BCB power is fixed (8 kW peak-power). We observe that the fraction of the output probe coupled to mode M_1 (M_2) is tuneable in the range 37-75% (30-70%).

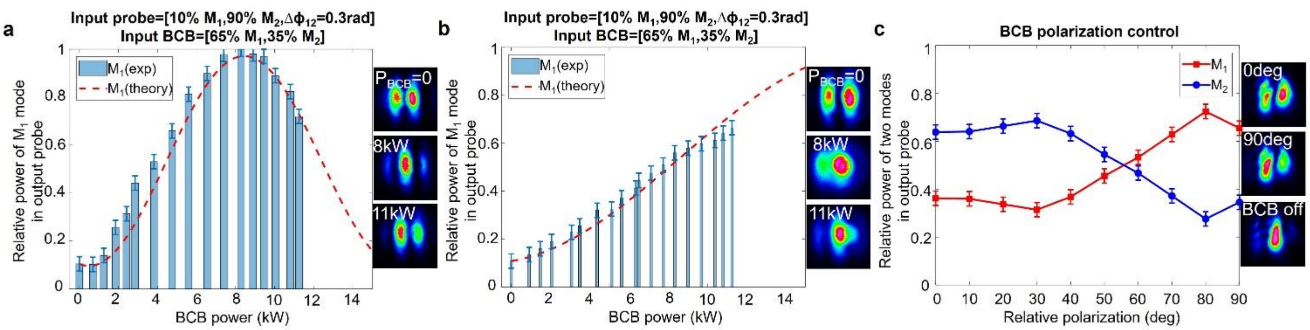

Fig. S3. Tuneable mode manipulation by adjusting the polarization. a,**b**. Comparison between output probe mode distribution in the co-polarized case (panel a) and orthogonally-polarized case (panel b). The insets show the far-field intensity of the output probe at different BCB power P_{BCB}. **c**. Mode distribution of the output probe as a function of the probe-BCB relative polarization for a fixed BCB power (8kW peak power). The insets show the far-field intensity at 0 deg, 90 deg and when BCB is turned off.

Supplementary Information 4: Linear VS nonlinear probe regime

The dynamics of the counter-propagating system, as described in equation (4) of the manuscript, are significantly influenced by the degree of nonlinearity of both the probe and BCB.

When both beams operate in a strongly nonlinear regime, the system exhibits asymptotic attraction to or rejection of specific mode states, as reported in Ref. S1. For instance, in the case of a bimodal fibre, the output probe beam is attracted towards the mode state orthogonal to the input BCB, and vice versa. In the example shown in Fig. S4a,b, we simulate a bimodal fibre with parameters L=1m, $\gamma_{11} = \gamma_{12} = \gamma_{22} = 1/W/km$. The input probe beam is entirely coupled to mode M_1, while the input BCB is distributed with 60% of its power in mode M_1 and 40% in mode M_2. The probe beam, with a total fixed peak power $P_p = 10$ kW, operates in a highly nonlinear regime (number of nonlinear lengths $L\gamma P_p = 10$, $\gamma = 1/W/km$ being the average Kerr coefficient). As the BCB's peak power increases from 0 to 10 kW, entering itself a strongly nonlinear regime, the mode attraction process outlined above occurs. Indeed, the output probe (Fig. S4a) tends to approach the mode state orthogonal to the input BCB, namely, ~ 40% on mode M_1 and ~ 60% on mode M_2. In turn, the output BCB (Fig. S4b) tends to approach the mode state orthogonal to the input probe, namely, all power coupled to mode M_2.

However, when the probe operates at a low peak power level, therefore remaining in a linear regime (which is the condition underlying the outcomes reported in the manuscript) the dynamics change drastically. The mode attraction process is not triggered. This is shown in Fig. S4c,d where the probe peak power is now arbitrary low (here P_p =0.01 kW, therefore the number of nonlinear lengths $L\gamma P_p = 0.01$). In this case, the output BCB's mode composition remains unchanged, mirroring the input (Fig. S4d). Meanwhile, the output probe mode distribution exhibits a sinusoidal evolution as the BCB power increases (Fig. S4c), in line with the predictions of our theoretical model (equation (1) in the manuscript) and the experimental outcomes reported in the manuscript.

The results shown in Fig. S4 are generalizable to fibres with arbitrary coefficients. As a rule of thumb, if the number of nonlinear lengths exceeds 5, then the probe operates in a strongly nonlinear regime, as depicted in Fig. S4a,b. Conversely, if it is below 0.5, then the probe operates in a linear regime, as illustrated in Fig. S4c,d.

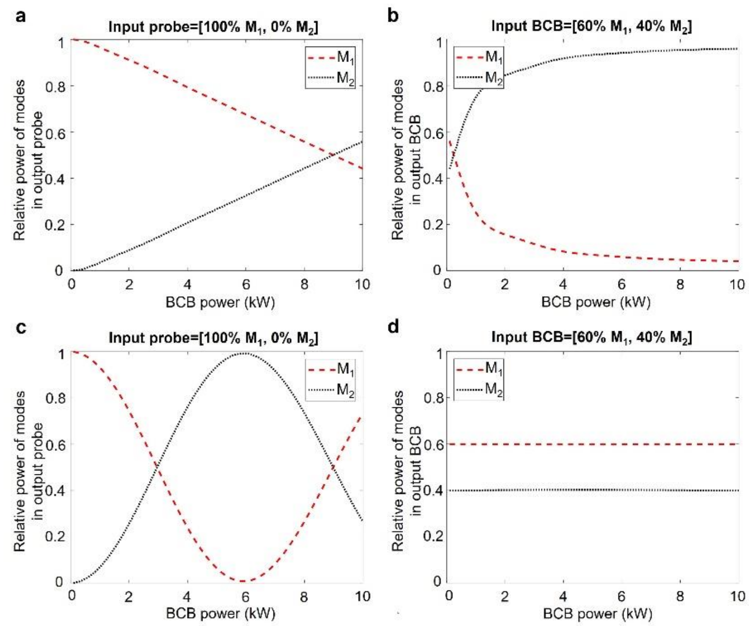

Fig. S4. Comparison between high power probe (mode attraction) and low power probe in a bimodal fibre. a-b. Mode distribution of the output probe (a) and output BCB (b) versus the BCB peak power when the probe is in a strong nonlinear regime (peak power fixed to 10 kW). The output probe is asymptotically attracted to the mode state orthogonal to the input BCB, and viceversa. **c-d**. Mode distribution of the output probe (c) and output BCB (d) versus the BCB peak power when the probe is in linear regime (peak power fixed to 0.01 kW). The output probe mode distribution oscillates sinusoidally as a function of the BCB power, whereas the BCB mode distribution is unchanged.

Supplementary Information 5: Ultrafast dynamics

In our experiments, we have demonstrated that the core-to-core power ratio of the output probe can be switched on a sub-nanosecond timescale (see Fig. 4c,d of the manuscript).

In the following, we discuss some numerical results that illustrate the core-to-core switching mechanism in detail. These results are obtained by simulation of the full CNLSEs reported in equation (4) of the manuscript. We focus on the case of pulsed BCB. For simplicity, we illustrate the case of a dual core fibre with L=1 m, $\gamma_{12} = 1/\mathrm{W/km}, \gamma_{11} = \gamma_{22} = 2/W/km$. The system under analysis possesses three critical timescales: the BCB pulse width τ_P; the BCB repetition rate R; and the time of flight $\tau_F = L/\mathrm{c}$ in the fibre (c= light velocity in the fibre). In these simulations, the BCB is equally distributed in the 2 fibre modes and the BCB pulse width τ_p=1 ps. Full core-to-core conversion (from 100/0 to 0/100) in the output probe is achieved for a BCB peak power P_{BCB} =6.2 MW. The probe peak power is instead arbitrary low.

Initially, we consider the case of a continuous-wave probe. In Fig. S5, we show the output probe temporal dynamics when the BCB is respectively off (Fig. S5b) and on (Fig. S5c). When the BCB is off, the output probe power is fully coupled to core 1 (100/0 power ratio). When the BCB is on, the first BCB pulse with P_{BCB} =6.2 MW (BCB pulse 1) triggers the full switching of the output probe power ratio from 100/0 to 0/100. This state is maintained over a time window $2\tau_F = 2L/c$, after which the power ratio returns to 100/0 (BCB off condition).

At the following BCB pulse (BCB pulse 2), after a time 1/R, the dynamics repeat. However, the peak power of BCB pulse 2 is now lower, i.e. 3.2 MW, resulting in a reduced conversion (45/55 power ratio). A similar dynamic applies to BCB pulse 3, whose low power results in a weak conversion (80/20 power ratio). Note that if the condition 1/R =$2\tau_F$ is met, then it is possible to maintain the output probe power ratio 0/100, as shown in Fig. S6.

Similar considerations apply when the probe is pulsed: regardless of the probe pulse width, each probe pulse within a time window of width $2\tau_F$ is switched, as reported in Fig. S7.

It is worth noting that the results illustrated above are generalizable to fibres with different parameters and/or more cores, as well as different pulse widths. Similarly, these results would extend to other waveguide systems beyond optical fibres. For example, using silicon-based integrated waveguides (which possess nonlinearities > 3 orders of magnitude higher than standard optical fibres), similar results to Figs. S5-S7 could be achieved but reducing the peak powers in the fraction-of-kW range. These peak power levels, along with ps pulses and GHz repetition rates, can be currently obtained using commercial fibre lasers. The combination of innovative all-optical pulse generation techniques (see Ref. S2) with our all-optical switching approach would underpin the development of an ultrafast all-optical integrated switching system.

Note finally that the switching time τ_{switch}, required to complete the core-to-core switching, is of the order of the BCB pulse width τ_p (see insets of Fig. S5). The latter is ultimately constrained by distortion due to interplay among dispersion and self-phase modulation, which poses a limit to the minimum BCB pulse width.

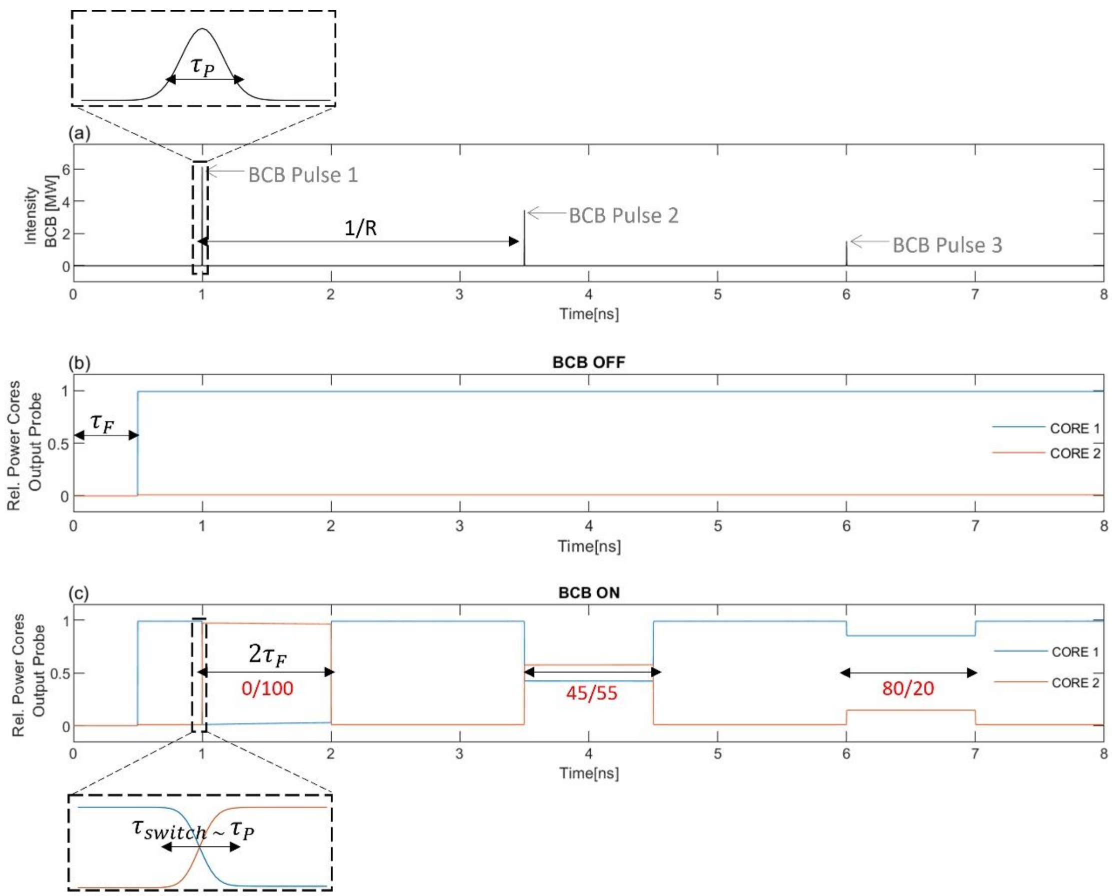

Fig. S5. Ultrafast dynamics with pulsed BCB, CW probe. Each BCB pulse (see panel a and related inset) causes a switching in the output probe core-to-core power ratio. The achieved power ratio (here 0/100, 45/55 and 80/20 for BCB pulses 1, 2 and 3, respectively) depends on the BCB pulse peak power. The switching is preserved over a time window of length $2\tau_F$, where the time of flight τ_F is shown in panel b.

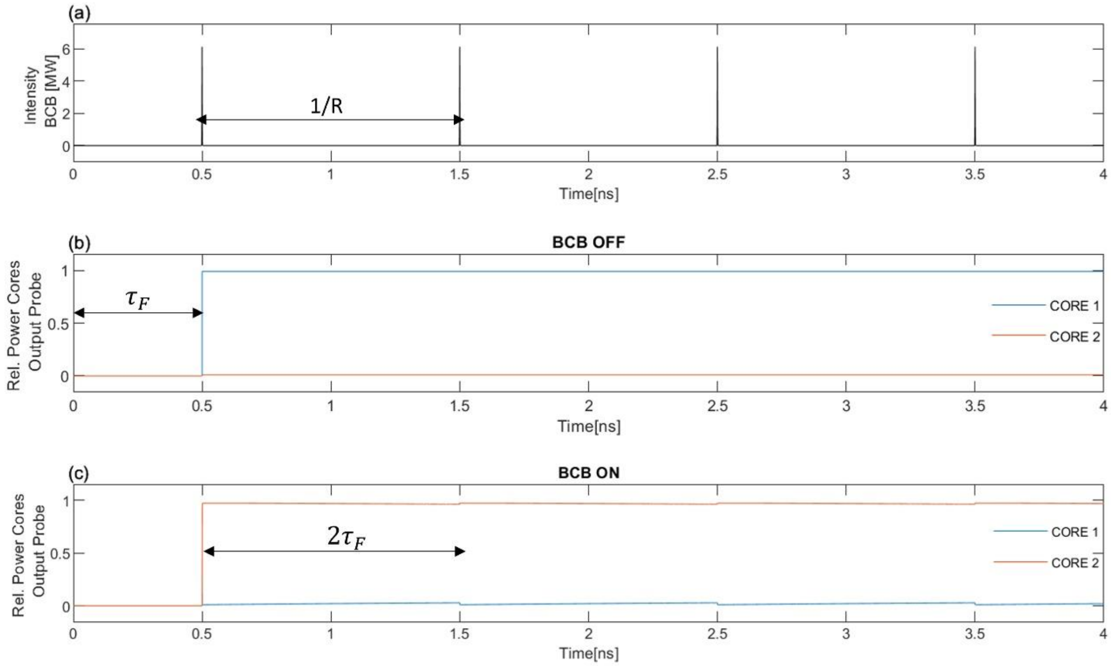

Fig. S6. Preserving 0/100 state. As Fig. S5, but here each BCB pulse has peak power 6.2 MW and the condition 1/R $=2\tau_F$ is met. Consequently, the output probe core-to- core power ratio 0/100 is preserved.

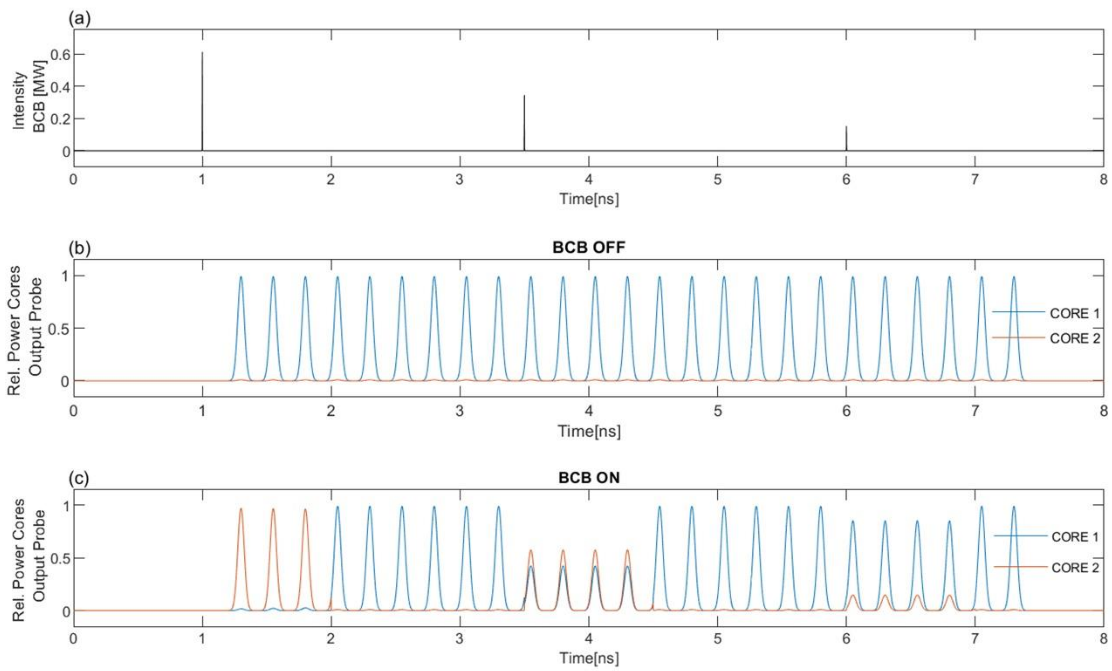

Fig. S7. Ultrafast dynamics with pulsed BCB, pulsed probe. As Fig. S5, but here the probe is pulsed with pulse width =200ps.

References

S1. Ji, K. H. *et al.* Mode attraction, rejection and control in nonlinear multimode optics. *Nat. Commun.* **14**, 7704 (2023).

S2. Berti, N., Coen, S., Erkintalo, M. & Fatome, J. Extreme waveform compression with a nonlinear temporal focusing mirror. *Nat. Photonics* **16**, 822-827 (2022).